Contact Conditions for Cylindrical, Prismatic, and Screw Joints in Flexible Multibody Systems *

O.A. Bauchau
Georgia Institute of Technology, School of Aerospace Engineering.
Atlanta, Georgia, 30332, USA.
Carlo L. Bottasso
Politecnico di Milano, Dipartimento di Ingegneria Aerospaziale.
Milano, Italy.

Abstract

This paper focuses on the modeling of the contact conditions associated with cylindrical, prismatic, and screw joints in flexible multibody systems. In the classical formulation these joints are developed for rigid bodies, and kinematic constraints are enforced between the kinematic variables of the two bodies. These constraints express the conditions for relative translation and rotation of the two bodies along and about a body-fixed axis, and imply the relative sliding and rotation of the two bodies which remain in constant contact with each other. However, these kinematic constraints no longer imply relative sliding with contact when one of the bodies is flexible. To remedy this situation, a *sliding joint* and a *sliding screw joint* are proposed that involves kinematic constraints at the instantaneous point of contact between the sliding bodies. For sliding screw joints, additional constraints are added on the relative rotation of the contacting bodies. Various numerical examples are presented that demonstrate the dramatically different behavior of cylindrical, prismatic, or screw joints and of the proposed sliding and sliding screw joints in the presence of elastic bodies, and the usefulness of these constraint elements in the modeling of complex mechanical systems.

1 Introduction

This paper is concerned with the dynamic analysis of flexible, nonlinear multibody systems, *i.e.* a collection of bodies in arbitrary motion with respect to each other as each body undergoes large displacements and rotations with respect to a body-fixed frame of reference. The focus is on problems where the strains within each elastic body remain small.

The elastic bodies are modeled using the finite element method. This paper focuses on beam elements. The location of each node of the beam is represented by its Cartesian coordinates in an inertial frame, and the rotation of the cross-section at each node is represented by a finite rotation tensor expressed in the same inertial frame. The kinematic constraints among the various bodies are enforced via the Lagrange multiplier technique. Although this approach does not involve the minimum set of coordinates, it allows a modular development of finite elements for the enforcement of the kinematic constraints.

A distinguishing feature of multibody systems is the presence of joints which impose different types of kinematic constraints between the various bodies of the system. An exhaustive classification

Multibody System Dynamics, **5**, pp 251–278, 2001.

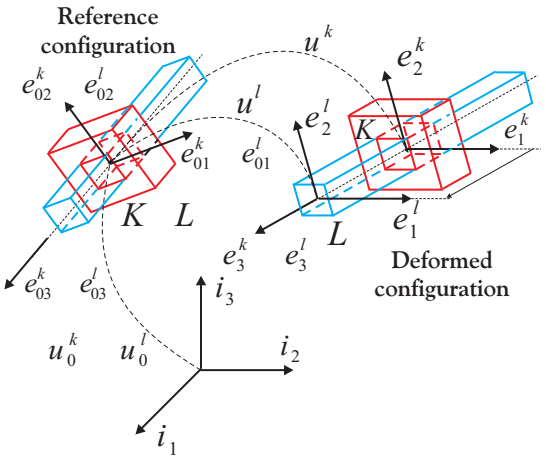

Figure 1: Prismatic joint in the reference and deformed configurations.

of these joint types can be found in text books, such as [1], for instance. This paper focuses on the modeling of cylindrical, prismatic, and screw joints. These three types of joints share the common characteristic of allowing relative translation between two bodies, together with possible relative rotation. In this introduction, the prismatic joint will be discussed as an example, the other two joints will be described in the body of the paper. The prismatic joint, schematically depicted in fig. 1, allows relative translation between two bodies, denoted body k and body l, about an axis fixed with respect to body k, while no relative rotation is allowed between the bodies.

At first, we consider the case where body l is a rigid body. Fig. 1 depicts the prismatic joint in the reference and deformed configurations. In the reference configuration, the prismatic joint is defined by coincident triads $\mathcal{S}_0^k = \mathcal{S}_0^l$, attached to points K and L, respectively, which are material points on bodies k and l, respectively. In the deformed configuration, the orientations of triads $\mathcal{S}^k$ and $\mathcal{S}^l$ are still identical, but their origins are different: body l translated a distance Δ with respect to body k in the direction $\mathbf{e}_3{}^k = \mathbf{e}_3{}^l$. The first set of kinematic constraints associated with the prismatic joint is

$$\underline{e}_1^{lT}\ \underline{u} = \underline{e}_2^{lT}\ \underline{u} = 0, \tag{1}$$

and imply the orthogonality of both $\mathbf{e}_1{}^l$ and $\mathbf{e}_2{}^l$ to $\mathbf{u} = \mathbf{u}^{\,l} - \mathbf{u}^{\,k}$, the vector joining points K and L. The second set of constraints reads

$$\underline{e}_1^k = \underline{e}_1^l; \quad \underline{e}_2^k = \underline{e}_2^l; \quad \underline{e}_3^k = \underline{e}_3^l, \tag{2}$$

which imply identical orientations for triads $\mathcal{S}^k$ and $\mathcal{S}^l$. Finally, the relative translation of the bodies is $\Delta = \underline{e}_3^{lT}\ \underline{u}$, the projection of vector $\mathbf{u}$ along $\mathbf{e}_3{}^l$. It is important to note that although these constraints are expressed in terms of the kinematic variables at points K and L, they imply the sliding of body l on body k at point K, *when body l is rigid*.

The situation is markedly different when body l is flexible, as shown in fig. 2. If conditions (1) and (2) are enforced, body l is no longer sliding on body k at point K, *i.e.* contact between the bodies is no longer enforced. In actual systems, the piece of hardware corresponding to the prismatic joint implies the sliding of body l on body k with contact at point K at all times, as depicted in fig. 3. In fact, in the presence of flexible bodies, such a joint is more accurately described as a *sliding joint*.

Due to the flexibility of body l, the kinematic variables at material points K and L are no longer related by conditions (1) and (2). Rather, constraint conditions must be enforced between the kinematic variables at point K of body k, and the kinematic variables at the material point of body l which is in contact with body k at a given instant. Clearly, the kinematic constraints, eq. (1)

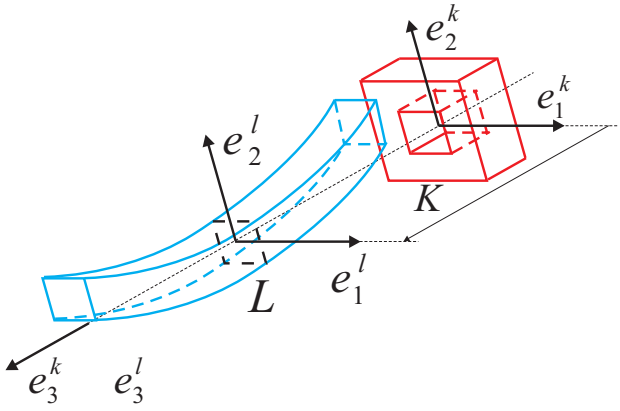

Figure 2: Prismatic joint with a flexible body.

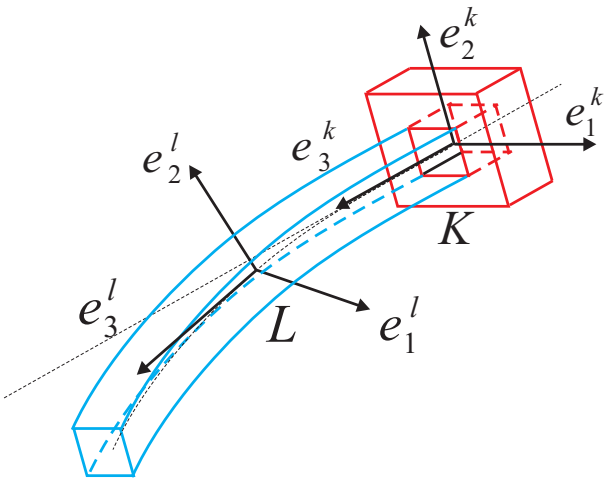

Figure 3: Sliding joint with a flexible body.

and (2) associated with the classical formulation of prismatic joints, and the kinematic constraint associated with sliding in the presence of flexible bodies are fundamentally different and will lead to sharply different dynamic responses of the system. Although the above discussion has focused on prismatic joints, it is clear that identical remarks can be made concerning the classical formulation of cylindrical and screw joints, and about their inadequacy to model sliding behavior in the presence of flexible bodies.

The nonlinear holonomic constraints associated with all the joints described in this work are formulated within the framework of the energy preserving [2, 3, 4, 5, 6] and decaying schemes [7, 8, 9, 10, 11, 12, 13, 14, 15] for multibody sytems. In these schemes, unconditional stability is achieved for nonlinear elastic multibody systems by combining two features: an energy preservation or decay statement for the elastic bodies of the system, and the vanishing of the work done by the forces of constraint. First, a discretization process for flexible members of the system is developed that preserves the total mechanical energy of the system at the discrete solution level. Then, a discretization process is proposed for the forces of constraint associated with the holonomic and non-holonomic constraints imposed on the system. Forces of constraint are discretized in a manner that guarantees the satisfaction of the nonlinear constraint manifold, *i.e.* the constraint condition will not drift. At the same time, the discretization implies the vanishing of the work performed by the forces of constraint at the discrete solution level. Consequently, the discrete energy conservation laws proved for the flexible members of the system are not upset by the introduction of the constraints. The resulting Energy Preserving (EP) scheme provides nonlinear unconditional stability for nonlinear, flexible multibody systems. However, it clearly lacks the indispensable high frequency numerical dissipation required to tackle realistic engineering problems [6].

In a second phase, a new discretization, closely related to that of the EP scheme, is developed for the flexible components of the system. This new discretization implies a discrete energy decay statement that results in high frequency numerical dissipation. The discretization of the forces of constraint is also closely related to that of the EP scheme and presents identical properties: no drift of the constraint conditions and vanishing of the work they perform. Here again, the introduction of constraints does not upset the discrete energy decay law. The resulting Energy Decaying (ED) scheme is therefore ideally suited for the simulation of nonlinear, flexible multibody systems with sliding joints whose dynamic response varies very rapidly due to the complex nature of the constraint conditions and to the moving contact point in sliding joints. An automated time step size selection procedure developed in [12] is used to obtain accurate solutions in an efficient manner.

This paper is organized in the following manner. The classical formulation of prismatic joints is described in section 3 and is followed in section 4 by the formulation of cylindrical and screw

joints which combine simpler joints, the universal and revolute joints. In section 5, the formulation of a simple, yet effective sliding joint is proposed. This joint involves the sliding of a node of a body along a flexible beam element and the rotations of the two bodies are not constrained in any manner. The sliding screw joint presented in section 6 involves an additional constraint on the relative rotation of the two bodies. Numerical examples are presented in section 7 that illustrate the sharp difference between the dynamic response of classical prismatic or screw joints and of the proposed sliding or sliding screw joints in the presence of flexible bodies.

2 Kinematic notation and conventions

The kinematic description of bodies and joints in their reference and deformed configurations will make use of three orthogonal triads. First, an inertial triad is used as a global reference for the system; it is denoted $\mathcal{S}_I$ with unit vectors $\mathbf{i}_1$, $\mathbf{i}_2$, and $\mathbf{i}_3$. A second triad $\mathcal{S}_0$, with unit vectors $\mathbf{e}_{01}$, $\mathbf{e}_{02}$, and $\mathbf{e}_{03}$ is attached to the body and defines its orientation in the reference configuration. Finally, a third triad $\mathcal{S}^*$ with unit vectors $\mathbf{e}_1$, $\mathbf{e}_2$, and $\mathbf{e}_3$ defines the orientation of the body in its deformed configuration.

Let $\mathbf{u}_0$ and $\mathbf{u}$ be the displacement vectors from $\mathcal{S}_I$ to $\mathcal{S}_0$, and $\mathcal{S}_0$ to $\mathcal{S}^*$, respectively, and $\mathbf{R}_0$ and $\mathbf{R}$ the rotation tensors from $\mathcal{S}_I$ to $\mathcal{S}_0$, and $\mathcal{S}_0$ to $\mathcal{S}^*$, respectively. In this work, all vector and tensor components are measured in either $\mathcal{S}_I$ or $\mathcal{S}^*$.

3 The prismatic joint

Consider two bodies denoted with superscripts $(.)^k$ and $(.)^l$, respectively, linked together by a prismatic joint, as depicted in fig. 1. In the reference configuration, the prismatic joint is defined by two coincident triads $\mathcal{S}_0^k = \mathcal{S}_0^l$. In the deformed configuration, no relative rotations are allowed and the corresponding triads are allowed to translate with respect to each other in such a way that ${\mathbf{e}_3}^k = {\mathbf{e}_3}^l$. This condition implies the orthogonality of both ${\mathbf{e}_1}^l$ and ${\mathbf{e}_2}^l$ to vector $\mathbf{u} = \mathbf{u}^{\,l} - \mathbf{u}^{\,k}$ which joins the origins of the two triads. These two kinematic constraints are

$$\mathcal{C}_\alpha = \underline{e}_\alpha^{lT}\ \underline{u} = 0, \tag{3}$$

with $\alpha = 1$ and 2, respectively. Of course, in the deformed configuration, the orientation of the two triads is still identical; this constraint is readily enforced within the framework of finite element formulations by Boolean identification of the corresponding degrees of freedom. The relative displacement Δ of the prismatic joint is defined by adding a third constraint

$$\mathcal{C}_3 = \underline{e}_3^{lT}\ \underline{u} - \Delta = 0, \tag{4}$$

which expresses the relative displacement of the bodies as the projection of $\mathbf{u}$ along ${\mathbf{e}_3}^l$. As discussed in [12], holonomic constraints are enforced by the addition of a constraint potential $\lambda\,\mathcal{C}$, where λ is the Lagrange multiplier. The forces of constraint $\underline{\mathcal{F}}^c$ corresponding to eqs. (3) or (4) are readily obtained as

$$\delta\mathcal{C}\lambda = \begin{bmatrix} \delta\underline{u}^k \\ \delta\underline{u}^l \\ \delta\underline{\psi}^l \\ \hline \delta\Delta \end{bmatrix}^T \begin{bmatrix} - & \lambda & \underline{e}_\alpha^l \\ & \lambda & \underline{e}_\alpha^l \\ & \lambda & \widetilde{e}_\alpha^l\ \underline{u} \\ - & \lambda & \end{bmatrix} = \begin{bmatrix} \delta\underline{u}^k \\ \delta\underline{u}^l \\ \delta\underline{\psi}^l \\ \hline \delta\Delta \end{bmatrix}^T \underline{\mathcal{F}}^c, \tag{5}$$

where the virtual rotations are defined as $\widetilde{\delta\psi} = (\delta R)\ R^T$, the virtual rotation vector is then denoted $\underline{\delta\psi}$; $\alpha = 1$, 2, and 3 for the three constraints, respectively; and the last line in the constraint force expression is omitted for the first two constraints. To obtain unconditionally stable schemes for

constrained systems, these forces of constraint must be discretized in time while enforcing that the work they perform vanishes exactly. To this effect, the difference between the constraint value in the final and initial configurations, denoted with subscripts $()_f$ and $()_i$, respectively, is evaluated below

$$\mathcal{C}_f - \mathcal{C}_i = (\underline{e}_{\alpha f}^{lT}\ \underline{u}_f - \Delta_f) - (\underline{e}_{\alpha i}^{lT}\ \underline{u}_i - \Delta_i). \tag{6}$$

The incremental rotation tensor R that rotates the unit vectors $\underline{e}_{\alpha i}^l$ to $\underline{e}_{\alpha f}^l$ is represented with Rodrigues parameters $\underline{r}$, see Appendix A. The use of identities (A6) then implies

$$\underline{e}_{\alpha f}^l = R\ \underline{e}_{\alpha f}^l = (I + \frac{\widetilde{r}}{2})\ \underline{e}_{\alpha m}^l; \quad \underline{e}_{\alpha i}^l = I\ \underline{e}_{\alpha i}^l = (I - \frac{\widetilde{r}}{2})\ \underline{e}_{\alpha m}^l. \tag{7}$$

Introducing these results into eq. (6) then yields

$$\mathcal{C}_f - \mathcal{C}_i = (\underline{u}_f^T - \underline{u}_i^T)\ \underline{e}_{\alpha m}^l + \underline{r}^T \widetilde{u}_m^T\ \underline{e}_{\alpha m}^l, \tag{8}$$

where

$$\underline{e}_{\alpha m}^l = \frac{\underline{e}_{\alpha f}^l + \underline{e}_{\alpha i}^l}{2}; \quad \underline{u}_m = \frac{\underline{u}_f + \underline{u}_i}{2}. \tag{9}$$

This result suggests the following time discretization of the constraint forces

$$\underline{\mathcal{F}}_m^c = \begin{bmatrix} - & s\lambda_m & \underline{e}_{\alpha m}^l \\ & s\lambda_m & \underline{e}_{\alpha m}^l \\ & s\lambda_m & \widetilde{e}_{\alpha m}^l\ \underline{u}_m \\ - & s\lambda_m & \end{bmatrix}, \tag{10}$$

where s is a scaling factor for the unknown, mid-point value of the Lagrange multiplier λ_m. In view of eq. (8), the work done by the constraint forces during the time step is $\Delta\mathcal{W}^c = s\lambda_m\ (\mathcal{C}_f - \mathcal{C}_i)$. Clearly, this work vanishes if $\mathcal{C}_f - \mathcal{C}_i = 0$. In order to avoid the drift phenomenon, it is preferable to enforce the condition $\mathcal{C}_f = 0$ at each time step. Consequently, the forces of constraint are discretized in time in a manner that guarantees the satisfaction of the nonlinear constraint manifold, *i.e.* the constraint condition will not drift. At the same time, the discretization implies the vanishing of the work performed by the forces of constraint at the discrete solution level. Consequently, the discrete energy conservation laws proved for the flexible members of the system are not upset by the introduction of the constraints. This energy preserving formulation can be readily extended to an energy decaying formulation by following the steps outlined in section 4.3 of [12].

The discretized forces of constraint, eq. (10), can be linearized to yield the Jacobian matrix of the constraints. Within the framework of the finite element formulation, this equivalent stiffness matrix is assembled with all other stiffness contributions of the system. The Lagrange multipliers are then explicitely computed at each time step.

4 The cylindrical and screw joints

The cylindrical and screw joints can be formulated as combinations of simpler joints, the universal, revolute and prismatic joints. Hence, the formulations of the universal and revolute joints will be discussed first.

4.1 The universal joint

Consider two bodies denoted with superscripts $(.)^k$ and $(.)^l$, respectively, linked together by a universal joint, as depicted in fig. 4. In the undeformed configuration, the universal joint is defined by two triads $\mathcal{S}_0^k$ and $\mathcal{S}_0^l$ with a common origin, and $\mathbf{e}_{03}^k$ is orthogonal to $\mathbf{e}_{03}^l$. The kinematic

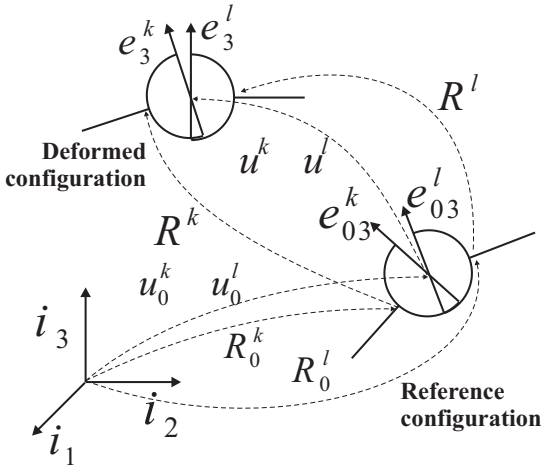

Figure 4: Universal joint in the undeformed and deformed configurations.

constraint associated with a universal joint implies the orthogonality of the corresponding vectors in the deformed configuration

$$\mathcal{C} = \underline{e}_\alpha^{kT}\ \underline{e}_\beta^{l} = g_{\alpha\beta} = 0, \tag{11}$$

where $\alpha = \beta = 3$. Here again, these holonomic constraints are enforced by the addition of a constraint potential $\lambda\,\mathcal{C}$, where λ is the Lagrange multiplier. The forces of constraint $\underline{\mathcal{F}}^c$ corresponding to eqs. (11) are

$$\delta\mathcal{C}\cdot\lambda = \left[\begin{array}{c} \delta\psi^k \\ \hline \underline{\delta\psi}^l \end{array}\right]^T \cdot \left[\begin{array}{ccc} & \lambda & \underline{h}_{\alpha\beta} \\ - & \lambda & \underline{h}_{\alpha\beta} \end{array}\right] = \left[\begin{array}{c} \delta\psi^k \\ \hline \underline{\delta\psi}^l \end{array}\right]^T \cdot \underline{\mathcal{F}}^c, \tag{12}$$

where

$$\underline{h}_{\alpha\beta} = \widetilde{e}_\alpha^{\,k}\ \underline{e}_\beta^{l}. \tag{13}$$

To obtain unconditionally stable schemes for constrained systems, these forces of constraint must be discretized in time while enforcing that the work they perform vanishes exactly. To this effect, the difference between the constraint value in the final and initial configurations is evaluated

$$\mathcal{C}_f - \mathcal{C}_i = g_{\alpha\beta f} - g_{\alpha\beta i} = \underline{e}_{\alpha f}^{kT}\ \underline{e}_{\beta f}^{l} - \underline{e}_{\alpha i}^{kT}\ \underline{e}_{\beta i}^{l}. \tag{14}$$

Introducing identities (7) then yields

$$\mathcal{C}_f - \mathcal{C}_i = (\underline{r}^{kT} - \underline{r}^{lT})\ \widetilde{e}_{\alpha m}^{k}\ \underline{e}_{\beta m}^{l} = (\underline{r}^{kT} - \underline{r}^{lT})\ \underline{h}_{\alpha\beta m}. \tag{15}$$

This result suggests the following discretization of the constraint forces

$$\underline{\mathcal{F}}_m^c = \left[\begin{array}{ccc} & s\lambda_m & \underline{h}_{\alpha\beta m} \\ - & s\lambda_m & \underline{h}_{\alpha\beta m} \end{array}\right]. \tag{16}$$

This discretization together with the constraint $\mathcal{C}_f = 0$ leads to the vanishing of the work done by the forces of constraint.

4.2 The revolute joint

Consider two bodies denoted with superscripts $(.)^k$ and $(.)^l$, respectively, linked together by a revolute joint, as depicted in fig. 5. In the undeformed configuration, the revolute joint is defined by coincident triads $\mathcal{S}_0^k = \mathcal{S}_0^l$. In the deformed configuration, no relative displacements are allowed

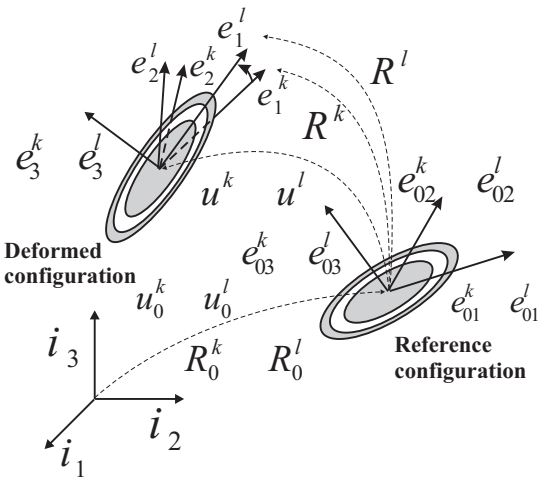

Figure 5: Revolute joint in the undeformed and deformed configurations.

and the corresponding triads are allowed to rotate with respect to each other in such a way that $\mathbf{e}_3{}^k = \mathbf{e}_3{}^l$. This condition implies the orthogonality of $\mathbf{e}_3{}^k$ to both $\mathbf{e}_1{}^l$ and $\mathbf{e}_2{}^l$. These two kinematic constraints are both given by eq. (11) with $\alpha = 3,\ \beta = 1$, and $\alpha = 3,\ \beta = 2$, respectively, and are enforced in the manner described in the previous section. The relative rotation ϕ between the two bodies is defined by adding to the revolute joint formulation a third constraint

$$\mathcal{C} = g_{\alpha\alpha} \sin\phi + g_{\alpha\beta} \cos\phi = 0, \tag{17}$$

where $\alpha = 1$ and $\beta = 2$. The corresponding forces of constraint $\underline{\mathcal{F}}^c$ are readily obtained

$$\delta\mathcal{C} \cdot \lambda = \begin{bmatrix} \delta\psi^k \\ \delta\psi^l \\ \delta\phi \end{bmatrix}^T \cdot \begin{bmatrix} \lambda & (\underline{h}_{\alpha\alpha} \sin\phi + \underline{h}_{\alpha\beta} \cos\phi) \\ -\lambda & (\underline{h}_{\alpha\alpha} \sin\phi + \underline{h}_{\alpha\beta} \cos\phi) \\ \lambda & (g_{\alpha\alpha} \cos\phi - g_{\alpha\beta} \sin\phi) \end{bmatrix} = \begin{bmatrix} \delta\psi^k \\ \delta\psi^l \\ \delta\phi \end{bmatrix}^T \cdot \underline{\mathcal{F}}^c. \tag{18}$$

The difference between the constraint value in the final and initial configurations is evaluated

$$\mathcal{C}_f - \mathcal{C}_i = (g_{\alpha\alpha f} \sin\phi_f + g_{\alpha\beta f} \cos\phi_f) - (g_{\alpha\alpha i} \sin\phi_i + g_{\alpha\beta i} \cos\phi_i). \tag{19}$$

Next, the following trigonometric identity is introduced

$$\begin{aligned} \sin\phi_f &= \frac{\sin\phi_f + \sin\phi_i}{2} + \frac{\sin\phi_f - \sin\phi_i}{2} = \sin_m\phi + \frac{1}{2} \frac{\sin\dfrac{\phi_f - \phi_i}{2}}{\dfrac{\phi_f - \phi_i}{2}} \left[\cos\frac{\phi_f + \phi_i}{2}\right] (\phi_f - \phi_i) \\ &= \sin_m\phi + \frac{S_m}{2} \cos\phi_m\ (\phi_f - \phi_i). \end{aligned} \tag{20}$$

One also finds $\sin\phi_i = \sin_m\phi - (S_m/2)\ (\cos\phi_m)\ (\phi_f - \phi_i)$, and similar relationships hold for the cosine function to yield

$$\begin{aligned} \mathcal{C}_f - \mathcal{C}_i &= (g_{\alpha\alpha f} - g_{\alpha\alpha i})\ \sin_m\phi + (g_{\alpha\beta f} - g_{\alpha\beta i})\ \cos_m\phi \\ &+ (g_{\alpha\alpha m}\ \cos\phi_m - g_{\alpha\beta m}\ \sin\phi_m)\ S_m\ (\phi_f - \phi_i). \end{aligned} \tag{21}$$

The terms in the two first parentheses are identical to eq. (14), and can be treated in a similar manner to yield

$$\begin{aligned} \mathcal{C}_f - \mathcal{C}_i &= (\underline{r}^{kT} - \underline{r}^{lT})\ (\sin_m\phi\ \underline{h}_{\alpha\alpha m} + \cos_m\phi\ \underline{h}_{\alpha\beta m}) \\ &+ (\phi_f - \phi_i)\ (g_{\alpha\alpha m}\ \cos\phi_m - g_{\alpha\beta m}\ \sin\phi_m)\ S_m, \end{aligned} \tag{22}$$

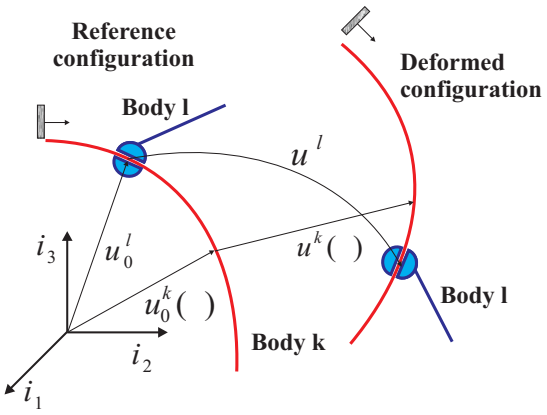

Figure 6: Sliding joint in the reference and deformed configurations.

where $g_{\alpha\beta m} = (g_{\alpha\beta f} + g_{\alpha\beta i})/2$. This result suggests the following discretization of the constraint forces

$$\underline{\mathcal{F}}_m^c = \begin{bmatrix} & s\lambda_m & (\underline{h}_{\alpha\alpha m} \ \sin_m \phi + \underline{h}_{\alpha\beta m} \ \cos_m \phi) \\ - & s\lambda_m & (\underline{h}_{\alpha\alpha m} \ \sin_m \phi + \underline{h}_{\alpha\beta m} \ \cos_m \phi) \\ & s\lambda_m & (g_{\alpha\alpha m} \ \cos \phi_m - g_{\alpha\beta m} \ \sin \phi_m) \end{bmatrix}, \tag{23}$$

This discretization together with the constraint $\mathcal{C}_f = 0$ leads to the vanishing of the work done by the forces of constraint.

4.3 The cylindrical joint

The cylindrical joint formulation is readily obtained by superposing the displacement constraints, eqs. (3) and (4), of the prismatic joint with the rotation constraints, eqs. (11) and (17), of the revolute joint. The two relative motions at the joint are the relative displacement Δ and the relative rotation ϕ.

4.4 The screw joint

Finally, the formulation of the screw joint is identical to that of the cylindrical joint, but a linear constraint is added between the relative displacement and rotation as

$$\mathcal{C} = \Delta - p \ \phi = 0, \tag{24}$$

where p is the pitch of the screw.

5 The sliding joint

Consider two bodies denoted with superscripts $(.)^k$ and $(.)^l$, respectively, linked together by a sliding joint, as depicted in fig. 6. Body k is a flexible beam element whose displacement field is interpolated from nodal quantities, using traditional finite element techniques. In the reference configuration, the coordinates of a point on the beam are

$$\underline{u}_0^k(\eta) = h^\alpha(\eta) \ \underline{u}_0^{k\alpha}, \tag{25}$$

where $\underline{u}_0^{k\alpha}$ are the coordinates of the nodal positions in the reference configuration, $h^\alpha(\eta)$ the shape functions used in the discretization of the beam element, $\eta \in [0, 1]$ a non-dimensional parameter

indicating the location of a material particle along the beam axis in the reference configuration, and α an integer varying from 0 to N, the number of nodes in the beam element. Summation over all nodes is implied by repeated α indices. The formulation of nonlinear beam elements is detailed in [12]. Body l can be a rigid or flexible element of the system. The position vector of a node point of this body is denoted $\underline{u}_0^l$ in the reference configuration.

After deformation, the position vector of a point on the beam becomes

$$\underline{P}^k(\eta) = h^\alpha(\eta)\ (\underline{u}_0^{k\alpha} + \underline{u}^{k\alpha}), \tag{26}$$

where $\underline{u}^{k\alpha}$ are the nodal displacement vectors. Similarly, the position vector of the node on body l is

$$\underline{P}^l = \underline{u}_0^l + \underline{u}^l, \tag{27}$$

where $\underline{u}^l$ is the nodal displacement vector. The kinematic constraint associated with the condition of body l freely sliding over the flexible beam is

$$\underline{\mathcal{C}} = \underline{P}^k(\eta) - \underline{P}^l = 0. \tag{28}$$

The parameter η which determines the location of contact between bodies k and l is, of course, a time-varying unknown of the problem. Here again, this constraint is enforced via the Lagrange multiplier technique. The corresponding forces of constraint $\underline{\mathcal{F}}^c$ are

$$\delta\underline{\mathcal{C}}^T\underline{\lambda} = \begin{bmatrix} \delta\underline{u}^{k\alpha} \\ \delta\eta \\ \delta\underline{u}^l \end{bmatrix}^T \begin{bmatrix} h^\alpha & \underline{\lambda} \\ h^{\alpha\,\prime}\ (\underline{u}_0^{k\alpha} + \underline{u}^{k\alpha})^T & \underline{\lambda} \\ - & \underline{\lambda} \end{bmatrix} = \begin{bmatrix} \delta\underline{u}^{k\alpha} \\ \delta\eta \\ \delta\underline{u}^l \end{bmatrix}^T \underline{\mathcal{F}}^c, \tag{29}$$

where $(.)'$ denotes a derivative with respect to η. To obtain unconditionally stable schemes for constrained systems, these forces of constraint must be discretized while enforcing that the work they perform vanishes exactly. To this effect, the difference between the constraint value in the final and initial configurations is evaluated

$$\mathcal{C}_f - \mathcal{C}_i = \left[h_f^\alpha\ (\underline{u}_0^{k\alpha} + \underline{u}_f^{k\alpha}) - (\underline{u}_0^l + \underline{u}_f^l)\right] - \left[h_i^\alpha\ (\underline{u}_0^{k\alpha} + \underline{u}_i^{k\alpha}) - (\underline{u}_0^l + \underline{u}_i^l)\right], \tag{30}$$

where $h_f^\alpha = h^\alpha(\eta_f)$. The following indentities are introduced

$$h_f^\alpha = \frac{h_f^\alpha + h_i^\alpha}{2} + \frac{h_f^\alpha - h_i^\alpha}{2} = h_m^\alpha + \frac{h_f^\alpha - h_i^\alpha}{2}; \quad h_i^\alpha = h_m^\alpha - \frac{h_f^\alpha - h_i^\alpha}{2}, \tag{31}$$

to yield

$$\mathcal{C}_f - \mathcal{C}_i = (\underline{u}_f^{k\alpha} - \underline{u}_i^{k\alpha})\ h_m^\alpha + (\eta_f - \eta_i)\ \frac{h_f^\alpha - h_i^\alpha}{\eta_f - \eta_i}\ (\underline{u}_0^{k\alpha} + \underline{u}_m^{k\alpha}) + (\underline{u}_f^l - \underline{u}_i^l). \tag{32}$$

This result suggests the following discretization of the constraint forces

$$\underline{\mathcal{F}}_m^c = \begin{bmatrix} h_m^\alpha & s\underline{\lambda}_m \\ \dfrac{h_f^\alpha - h_i^\alpha}{\eta_f - \eta_i}\ (\underline{u}_0^{k\alpha} + \underline{u}_m^{k\alpha})^T & s\underline{\lambda}_m \\ - & s\underline{\lambda}_m \end{bmatrix}, \tag{33}$$

This discretization together with the constraint $\mathcal{C}_f = 0$ leads to the vanishing of the work done by the forces of constraint.

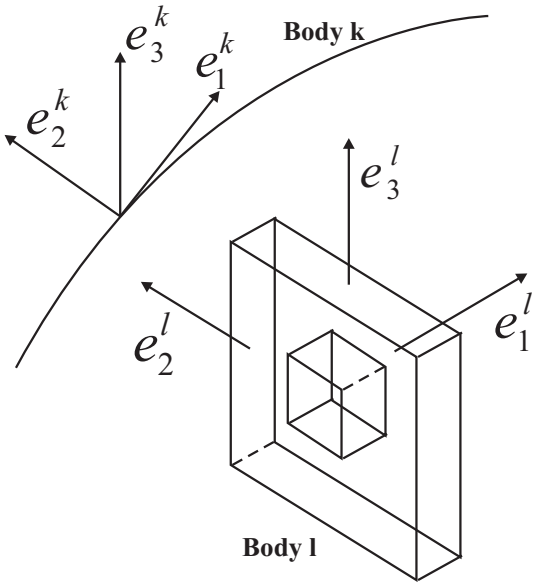

Figure 7: Definition of orientations on bodies k and l for a sliding screw joint.

6 The sliding screw joint

It should be noted that the kinematic constraints associated with the sliding joint do not involve the rotational degrees of freedom of bodies k and l. In some cases, the rotation of body l might be constrained to match the twist of the beam, body k. Let the unit vectors $\underline{e}_2^k$ and $\underline{e}_3^k$ define the plane of the cross section of the beam, and $\underline{e}_\alpha^l$ define a triad attached to body l, as depicted in fig. 7. If the rotation of body l is constrained to follow the twist of beam k, the following constraint must be enforced

$$\mathcal{C} = \underline{e}_2^{kT}(\eta)\ \underline{e}_3^l = 0. \tag{34}$$

This constraint is similar to that corresponding to the universal joint, eq.(11). However, an important difference exists: the unit vector $\underline{e}_2^k$ is a function of η, *i.e.* as body l slides along the beam k, it must rotate to match the local twist of the beam at the instantaneous point of contact whose location is defined by η. In other words, this constraint is equivalent to a universal joint attached to body l and to a point sliding along body k. The forces of constraint $\underline{\mathcal{F}}^c$ corresponding to eqs. (34) are

$$\delta\mathcal{C}\cdot\lambda = \begin{bmatrix} \underline{\delta\psi}^{k\alpha} \\ \delta\eta \\ \underline{\delta\psi}^{l} \end{bmatrix}^T \begin{bmatrix} \lambda & h^\alpha \widetilde{e}^{\,k}\ \underline{e}^l \\ \lambda & \underline{e}^{lT}\ \widetilde{e}^{\,k}\ \underline{\kappa} \\ \lambda & \widetilde{e}^{\,l}\ \underline{e}^k \end{bmatrix} = \begin{bmatrix} \underline{\delta\psi}^{k\alpha} \\ \delta\eta \\ \underline{\delta\psi}^{l} \end{bmatrix}^T \underline{\mathcal{F}}^c, \tag{35}$$

where $\widetilde{\kappa} = R'R^T$ is the beam curvature vector, and the notation $()'$ indicates a derivative with respect to η. To obtain unconditionally stable schemes for constrained systems, these forces of constraint must be discretized while enforcing that the work they perform vanishes exactly. To this effect, the difference between the constraint value in the final and initial configurations is evaluated

$$\mathcal{C}_f - \mathcal{C}_i = \underline{e}_f^{kT}(\eta_f)\ \underline{e}_f^l - \underline{e}_i^{kT}(\eta_i)\ \underline{e}_i^l, \tag{36}$$

where the subscripts $()_2$ and $()_3$ have been dropped for simplicity. First, we introduce identity (7) for vectors $\underline{e}_f^l$ and $\underline{e}_i^l$ to find

$$\mathcal{C}_f - \mathcal{C}_i = \underline{r}^{lT}\ \widetilde{e}_m^l\ \underline{e}_{mm}^k + \underline{e}_m^{lT}\ [\underline{e}_f^k(\eta_f) - \underline{e}_i^k(\eta_i)]. \tag{37}$$

where $\underline{e}^k_{mm} = \underline{e}^k_f(\eta_f) + \underline{e}^k_i(\eta_i)$. Next, the same identities are introduced for vectors $\underline{e}^k_f$ and $\underline{e}^k_i$

$$\mathcal{C}_f - \mathcal{C}_i = \underline{r}^{lT}\ \widetilde{e}^l_m\ \underline{e}^k_{mm} + \underline{e}^{lT}_m\ (\underline{e}^k_{mf} - \underline{e}^k_{mi}) + \underline{e}^{lT}_m\ \frac{1}{2}[\widetilde{r}_f\ \underline{e}^k_{mf} + \widetilde{r}_i\ \underline{e}^k_{mi}], \tag{38}$$

where $\underline{e}^k_{mf} = [\underline{e}^k_f(\eta_f) + \underline{e}^k_i(\eta_f)]/2$ and $\underline{e}^k_{mi} = [\underline{e}^k_f(\eta_i) + \underline{e}^k_i(\eta_i)]/2$, and $\underline{r}_i = \underline{r}(\eta_i)$, $\underline{r}_f = \underline{r}(\eta_f)$ are the Rodrigues parameters measuring the beam incremental rotations at η_i and η_f, respectively. This result suggests the following discretization of the constraint forces

$$\underline{\mathcal{F}}^c_m = \begin{bmatrix} - & s\lambda_m & \left[\widetilde{e}^k_{mf}\ h^\alpha_f + \widetilde{e}^k_{mi}\ h^\alpha_i\right]/2\ \underline{e}^l_m \\ & s\lambda_m & \underline{e}^{lT}_m\ \dfrac{\underline{e}^k_{mf} - \underline{e}^k_{mi}}{\eta_f - \eta_i} \\ & s\lambda_m & \widetilde{e}^l_m\ \underline{e}^k_{mm} \end{bmatrix}, \tag{39}$$

This discretization together with the constraint $\mathcal{C}_f = 0$ leads to the vanishing of the work done by the forces of constraint.

7 Numerical examples

All the numerical examples presented in this sections used the energy decaying scheme described in [11, 12]. This scheme provides unconditional stability for nonlinear multibody systems involving both prismatic and sliding joints. An automated time step size selection procedure developed in [12] was used to obtain accurate solutions in an efficient manner.

7.1 The beam slider problem

The first numerical example is the beam slider problem that will be used to illustrate the dramatic difference between prismatic and sliding joints when flexible bodies are involved. Fig. 8 depicts the problem configuration: a flexible beam of length $L = 2.4\ m$ is pinned at point R by means of a spherical joint, and carries a tip body of mass $M_T = 40\ Kg$ and moments of inertia $I_{11} = 2I_{22} = 2I_{33} = 0.45\ Kg.m^2$. A driver of height $h = 1.6\ m$ is pinned at point A by means of a revolute joint with its axis of rotation along $\imath_3$ and is connected to the beam at point B. Two cases will be investigated, denoted *cases 1* and *2*, respectively. The driver is connected to the beam by means of a sliding joint for *case 1*, and a prismatic joint connected to a revolute joint with its axis of rotation along $\mathbf{i}_3$ for *case 2*. The relative translation at the sliding joint is prescribed as $\eta = 0.5 - 0.25\ \cos 2\pi t$, whereas that of the prismatic joint is prescribed as $\Delta = 0.6\ (1 - \cos 2\pi t)\ m$. Note that the prescribed motions for *cases 1* and *2* are identical, the different expressions for Δ and η reflect their different definitions. The beam and driver were modeled with 12 and 3 cubic beam elements, respectively. The rather fine mesh used for the beam is necessary because the sliding joint corresponds to a point load traveling along the beam. Although this fine mesh was not required for *case 2* which converged with 4 elements only, the same fine mesh was used for both cases. The physical properties of the beam are: axial stiffness $EA = 44.0\ MN$, bending stiffnesses $EI_{22} = 300.0$ and $I_{33} = 23.0\ KN.m^2$, torsional stiffness $GJ = 28.0\ KN.m^2$, shearing stiffnesses $GK_{22} = 2.8$ and $GK_{33} = 14.0\ MN$, mass per unit span $m = 1.6\ Kg/m$, and mass moment of inertia per unit span $I_{22} = 1.0$ and $I_{33} = 11.0\ mg.m$. The properties of the driver are identical to those of the beam except for the following quantities: bending stiffnesses $EI_{22} = 23.0$ and $I_{33} = 300.0\ KN.m^2$, and shearing stiffnesses $GK_{22} = 14.0$ and $GK_{33} = 2.8\ MN$.

The system was simulated for a period of 2 *sec*. Figs. 9 and 10 depict the beam tip vertical displacement and rotation, respectively. Note the sharp difference between the two cases; for *case 1* a very significant high-frequency content is apparent in the response. The beam mid-span axial

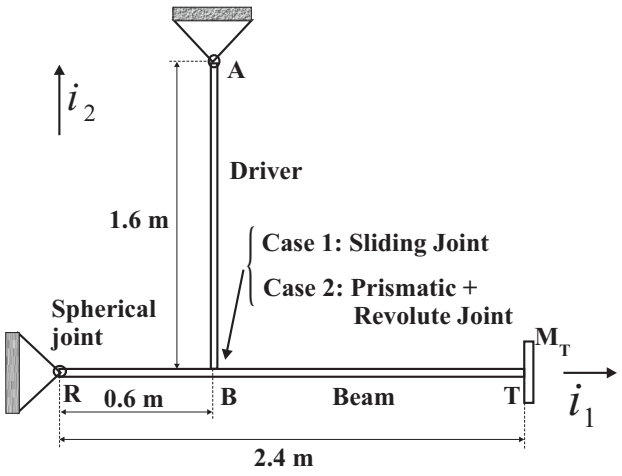

Figure 8: The beam slider problem.

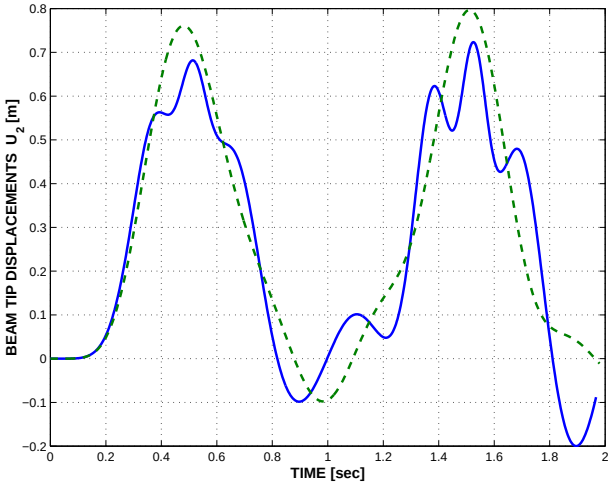

Figure 9: Time history of beam vertical tip displacement u_2. *Case 1:* solid line; *case 2:* dashed line.

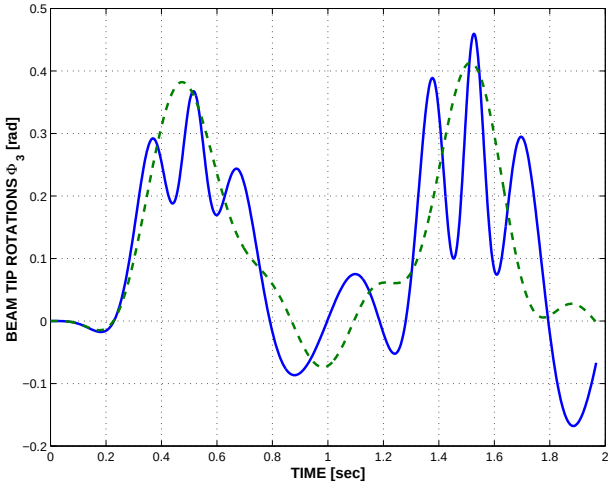

Figure 10: Time history of beam tip rotation Φ_3. *Case 1:* solid line; *case 2:* dashed line.

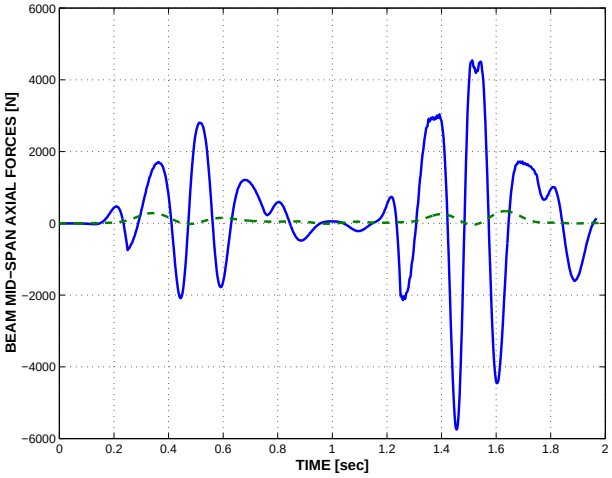

Figure 11: Time history of beam mid-span axial force F_1. *Case 1:* solid line; *case 2:* dashed line.

force is shown in fig. 11. The axial force for *case 1* is about 20 times larger than that in *case 2*, and peaks at times $t = 0.5$ and 1.5 *sec*, *i.e* when the slider contacts the beam at its mid-span. This phenomenon is absent for *case 2* since the prismatic joint remains attached to the fixed point B on the beam, *i.e.* the interaction force between the driver and the beam does not slide along the beam.

Fig. 12 depicts the beam mid-span bending moment time history. The peak value for *case 1* is about 30% higher than for *case 2*. It is interesting to note the variable frequency response for *case 1*: the period of the response around time $t = 1$ *sec* is about twice that of the response at time $t = 1.5$ *sec*. This is due to the variable geometry of the problem in the presence of the sliding joint: the driver provides a point support to the beam at a point that moves along its span. In contrast, the frequency of the response for *case 2* is nearly constant because the driver remains attached to the beam at the fixed point B. The same remarks can be made about the driver mid-span axial force shown in fig. 13. The peak axial force is about four times larger for *case 1*.

Finally, the force required to drive the sliding or prismatic joint is depicted in fig. 14. The same remark apply here again, and the peak value of the driving force is about six times larger for *case 1*.

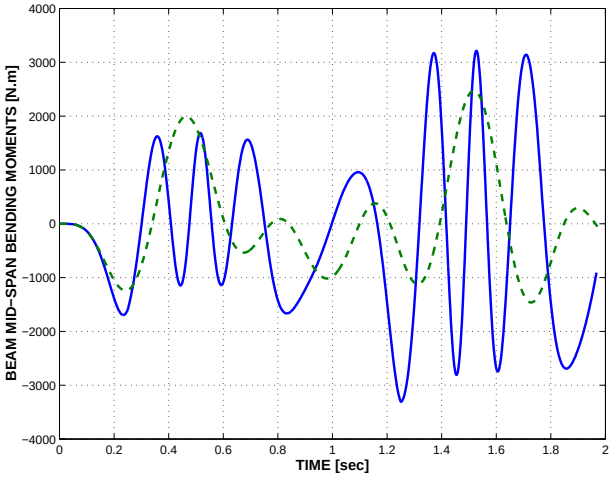

Figure 12: Time history of beam mid-span bending moment M_3. *Case 1:* solid line; *case 2:* dashed line.

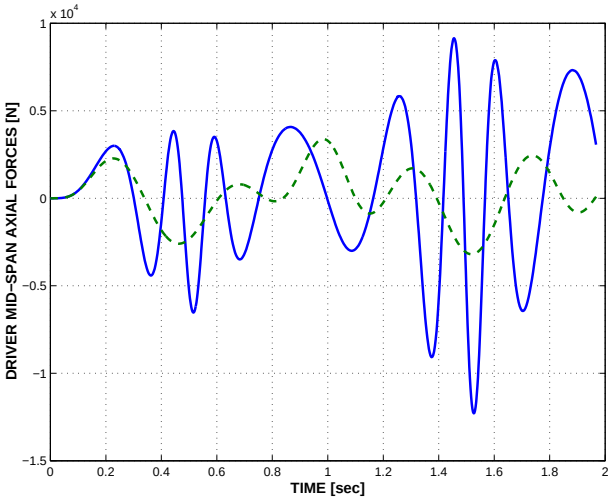

Figure 13: Time history of driver mid-span axial force F_1. *Case 1:* solid line; *case 2:* dashed line.

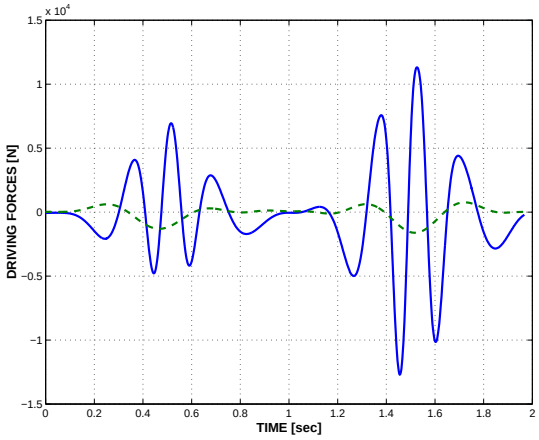

Figure 14: Time history of the driving force. *Case 1:* solid line; *case 2:* dashed line.

7.2 The twisted beam slider problem

The configuration of the second numerical example is identical to that the first example, except for one important difference: the beam is now pre-twisted with a constant twist rate $k_1 = 0.4363\, rad/m$. In *case 1*, the driver is connected to the beam by means of a sliding screw joint which rotates according to the beam twist. The relative translation at the sliding screw joint is prescribed as $\eta = 0.5 - 0.25 \cos 2\pi t$. For *case 2*, the driver is connected to the beam by means of a screw joint followed by a universal joint. The relative translation of the screw joint is prescribed as $\Delta = 0.6\ (1 - \cos 2\pi t)\ m$, and the pitch of the screw is $p = 1/k_1$, *i.e.* is matches the pre-twist of the beam. The universal joint transfers the sole relative rotation of the screw joint to the driver. The system is simulated for a total of 3 *sec*.

Due to the presence of the sliding screw joint moving along a twisted beam, the response of the system is now three-dimensional, as can be seen in figs. 15 and 16, which depict the beam tip transverse displacement and twist, respectively. Here again the displacements and rotations for *case 1* are found to be much larger than for *case 2*, up to 2.5 times for the tip twist. The responses for the beam mid-span axial forces shown in fig. 17 differ in both amplitude and frequency for *cases 1* and *2*.

Due to the three-dimensional nature of the motion, a large out-of-plane transverse shearing force

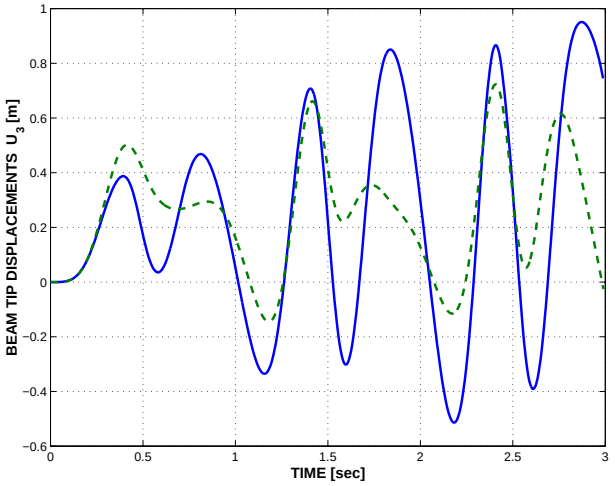

Figure 15: Time history of the beam tip out-of-plane displacement u_3. *Case 1:* solid line; *case 2:* dashed line.

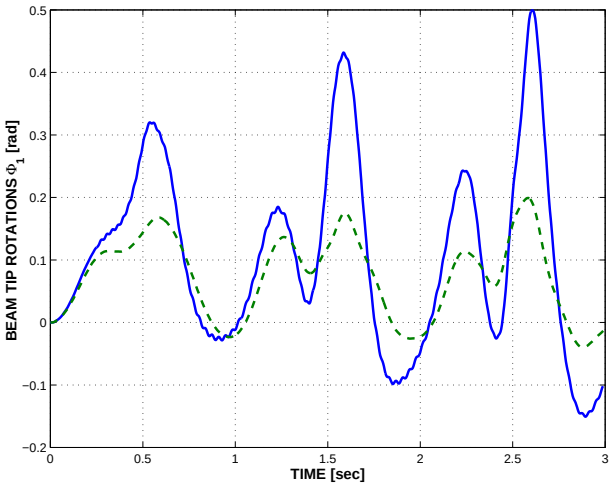

Figure 16: Time history of the beam tip twist ϕ_1. *Case 1:* solid line; *case 2:* dashed line.

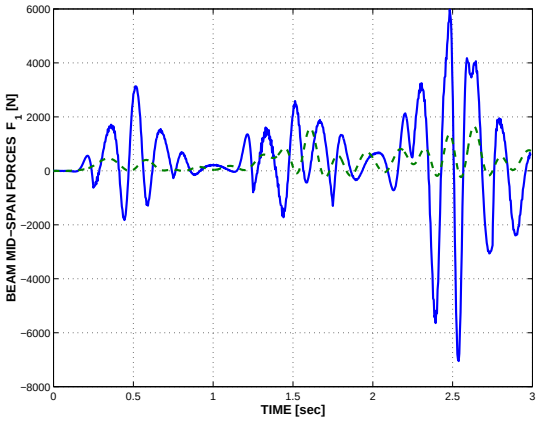

Figure 17: Time history of the beam mid-span axial force F_1. *Case 1:* solid line; *case 2:* dashed line.

develops in the beam and is depicted in fig. 18. The most dramatic difference between the two cases is found in the beam mid-span torque shown in fig. 19. For *case 1*, large mid-span torques are observed at times $t = 0.5$, 1.5, and 2.5 *sec*, *i.e.* when the slider contacts the beam at its mid-span. For *case 2*, the torque remains very small at all times and is uniquely due to torsional inertial effects in the beam.

The driver mid-span axial force is shown in fig. 20; here again sharp differences are observed in both amplitude and frequency of the response for *cases 1* and *2*. Finally, the force required to drive the sliding or cylindrical joint is depicted in fig. 21; the peak value of the driving force is about five times larger for *case 1*.

7.3 The variable diameter rotor problem

The last example deals with the modeling of a variable diameter tilt-rotor (VDTR) aircraft. The purpose of the example is to demonstrate the use of sliding and sliding screw joints in the modeling of practical problems of engineering interest. Tilt-rotors are machines ideally suited to accomplish vertical take-off and landing missions characterized by high speed and long range. They operate either as a helicopter or as a propeller driven aircraft. The transition from one mode of operation to

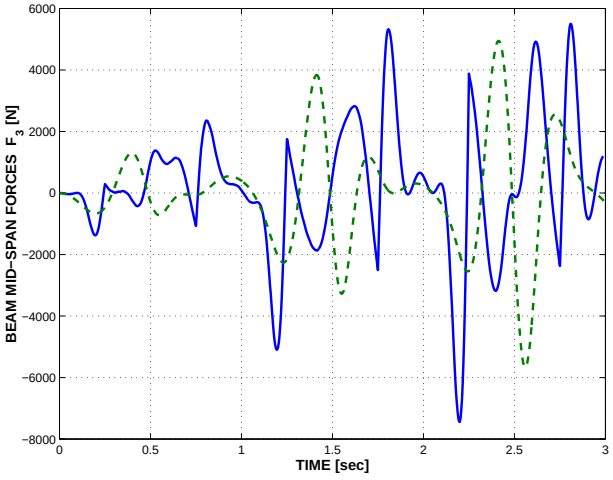

Figure 18: Time history of the beam mid-span out-of-plane shearing force F_3. *Case 1:* solid line; *case 2:* dashed line.

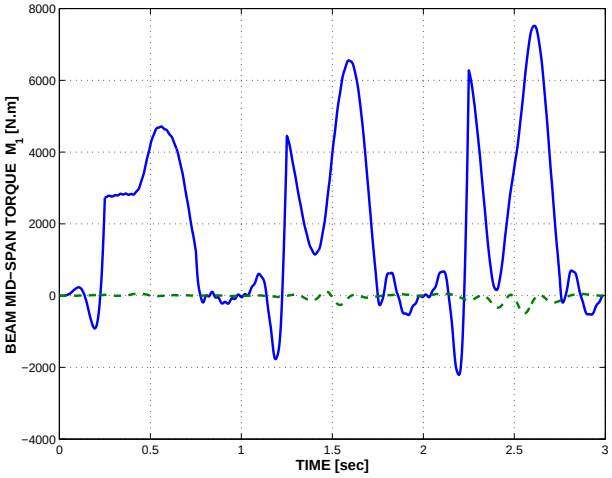

Figure 19: Time history of the beam mid-span torque M_1. *Case 1:* solid line; *case 2:* dashed line.

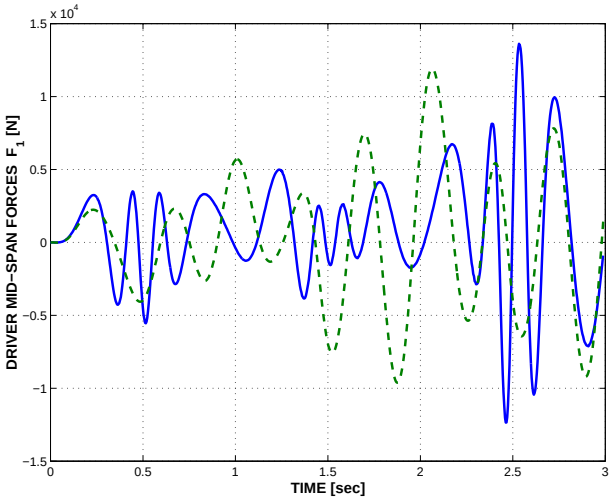

Figure 20: Time history of the driver mid-span axial force F_1. *Case 1:* solid line; *case 2:* dashed line.

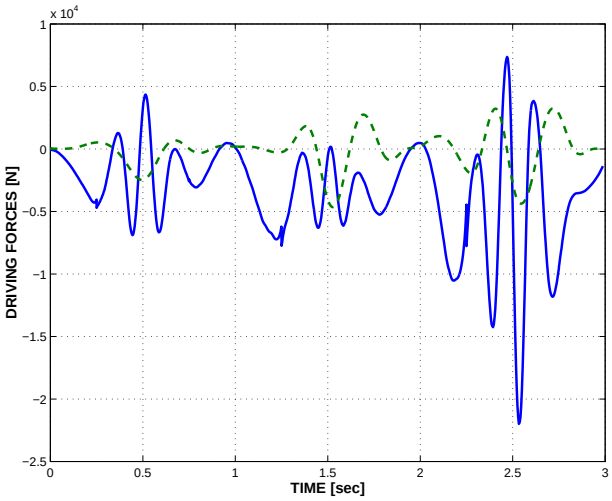

Figure 21: Time history of the driving force. *Case 1:* solid line; *case 2:* dashed line.

the other is achieved by tilting the engine nacelles. VDTR's further refine the tilt-rotor concept by introducing variable span blades to obtain optimum aerodynamic performance in both hover and cruise configurations. A general description of current VDTR technology is given in [16]. A design schematic of a typical VDTR is shown in fig. 22.

VDTR's are fairly complex machines. The main components of the rotor system are the gimbal, the blade hinges and the swashplate with the control linkages. Fig. 23 presents the Sikorsky telescoping blade design. A detailed description of the functionality of the different components of a VDTR are beyond the objectives of the present paper. Our interest here is in the fact that the proper modeling of several key parts of the rotor system and of the blade requires the use of sliding joints. Fig. 24 presents a multibody model of a typical VDTR configuration where a single blade only is shown, for clarity. A sliding joint and a sliding screw joint connect the swashplate and the shaft. The motion of the swashplate along the shaft controls the blade pitch through the pitch linkages. Prescribing the relative translation of the sliding joint, *i.e* the translation of the swashplate with respect to the shaft controls the pitch setting, effectively tranferring the pilot's command in

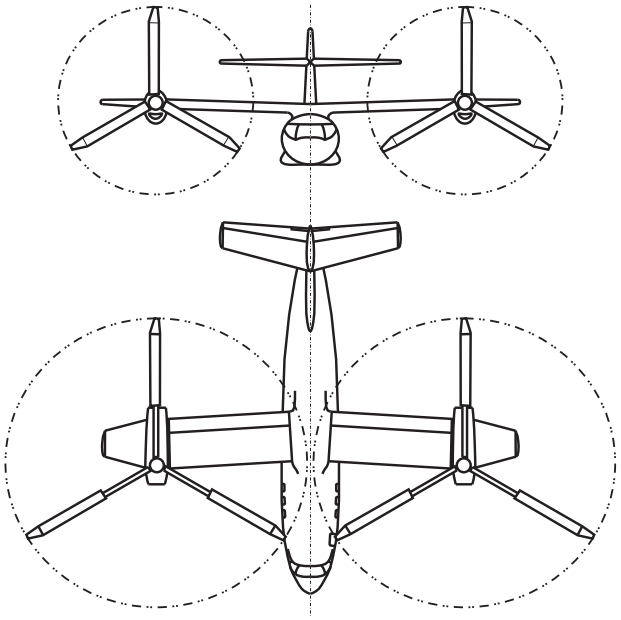

Figure 22: VDTR design schematic. Top figure: cruise configuration; bottom figure: hover configuration.

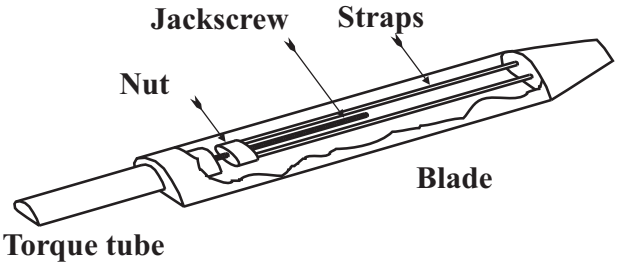

Figure 23: The Sikorsky telescoping blade design.

the stationary system to the blade in the rotating system. The presence of a screw joint forces the swashplate to rotate with the shaft while sliding along it. This is usually accomplished in a real system with a scissor-like mechanism that connects swashplate and shaft. This level of detail in the model, although possible using beams and/or rigid bodies and revolute joints, is not required for the present analysis. A sliding screw joint models the nut-jackscrew assembly. The motion of the nuts along the jackscrew allows the variation of the blade span in a continuous manner. By prescribing the relative translation at the joint we can then deploy or retract the blade according to a suitable function of the nacelle tilt. Finally, sliding screw joints are used to model the distributed sliding contact between the torque tube and the outboard blade. Note that a sliding screw joint must be used here as the pilot's input is transferred from the translation of the swashplate to the twisting of the torque tubes through the pitch links, and finally to twisting of the outboard blade. Appropriate springs and dampers are provided at the gimbal, while springs are present at the flap and lag revolute joints in order to correctly represent the characteristics of the system.

The VDTR rotor is initially in the hover configuration, with the nacelles tilted upwards and the blades fully deployed. The rotor angular velocity is equal to 20 rad/sec. The shaft rotational speed and blade pitch setting are kept constant while the nacelle is tilted forward to reach the cruise configuration. At the same time, the blades are retracted to avoid impact between the blade tips and the fuselage, and to optimize aerodynamic performance. The maneuvre is completed in 20 sec, corresponding to about 64 revolutions of the rotor. The time history of the relative prescribed rotation at the wing-nacelle revolute joint is given as $\varphi = 0.25\,\pi\,(1 - \sin(2\,\pi(t/40 + 0.25))$, while the prescribed displacement at the nut-jackscrew sliding joint is linear in time. The retracted rotor diameter for cruise mode is 66% of that in hover. This simulation was conducted in a vacuum, *i.e.* without aerodynamic forces acting on the blades.

Fig. 25 gives a three-dimensional view of the trajectory of the tip of one of the blades throughout the maneuvre. This view is deceptively simple. In fact, the tilting of the nacelle involves a complex tilting motion of the gimbal with respect to the shaft. In turns, flapping, lagging and pitching motions of the blades are excited. The time history of one of the relative rotations at the gimbal is presented in Fig. 26. The rotation about the other axis of the universal joint presents a similar

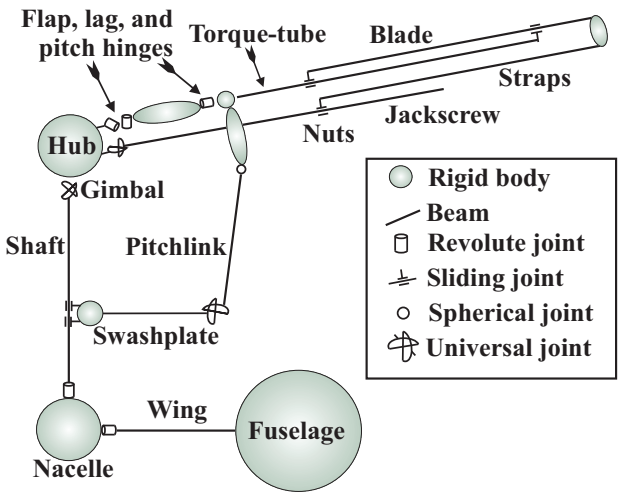

Figure 24: Multibody model of a VDTR (For clarity, a single blade only is shown.)

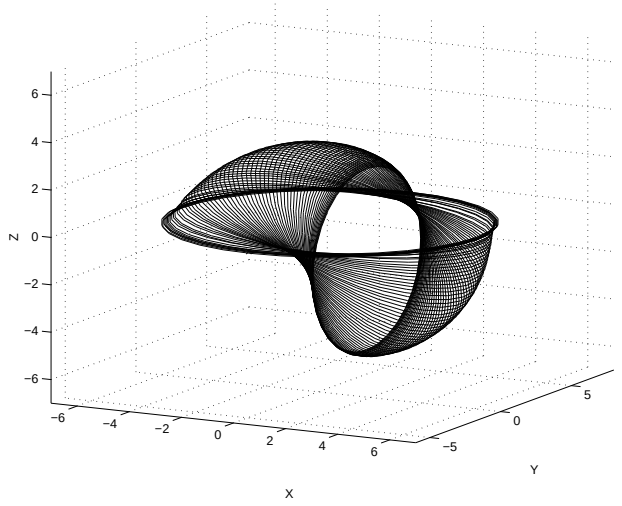

Figure 25: Tip blade trajectory for the conversion from helicopter to cruise mode of a VDTR.

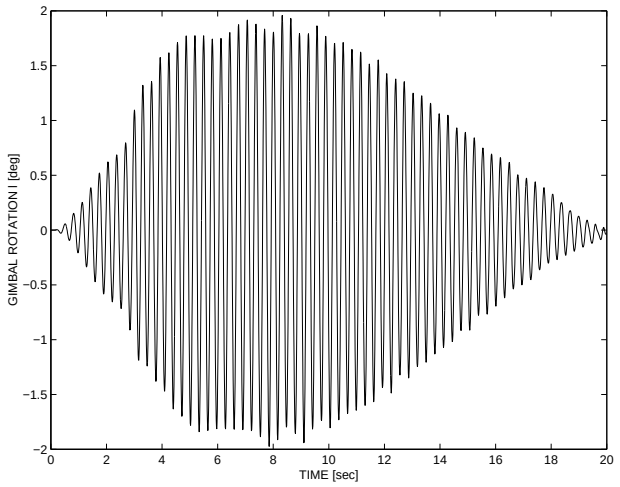

Figure 26: Time history of one of the relative rotations at the rotor gimbal.

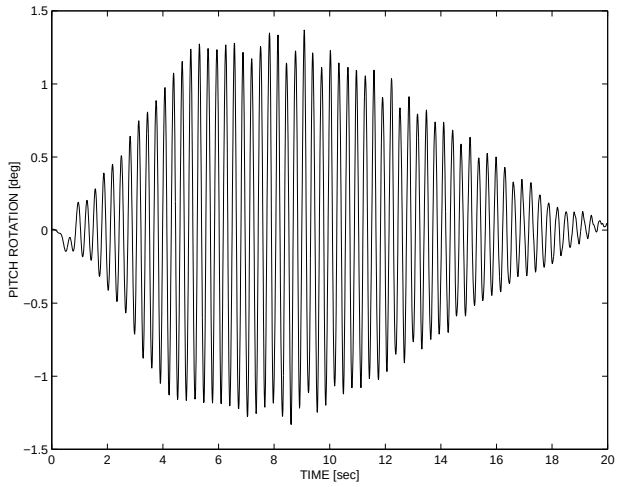

Figure 27: Time history of the relative rotations at the pitch hinge.

behavior. As the nacelle begins its motion, gimbal rotations are excited and sharply increase during the first half of the conversion process. Then, the dampers present in the universal joint progressively decrease the amplitude of this motion. Fig. 27 shows the time history of the blade pitch. This pitching is entirely due to the gimbal tilting, since the swashplate location along the shaft was fixed, which would imply a constant value of pitch for a rigid system. As expected, this motion closely follows the behavior of the gimbal. Fig. 28 shows the time history of lag hinge rotation, which appears to be undamped. This is to be expected since there are no dampers in the lag hinges. Such motion would of course be damped by the aerodynamic forces.

Fig. 29 shows the time history of the force at the jackscrew-nut sliding joint during the blade retraction. Note that the jackscrew carries the entire centrifugal force. Indeed, the blade is free to slide with respect to the torque tube, and hence, no axial load is transmitted to this member. As a result, the variable span blade is subjected to compression during operation, a radical departure from classical designs in which blades operate in tension. As expected, fig. 29 shows that the axial load in the jackscrew decreases as the rotor diameter is reduced. The high frequency oscillating components of the signal are once again due to the flapping, lagging and tilting motions of blades and gimbal discussed above.

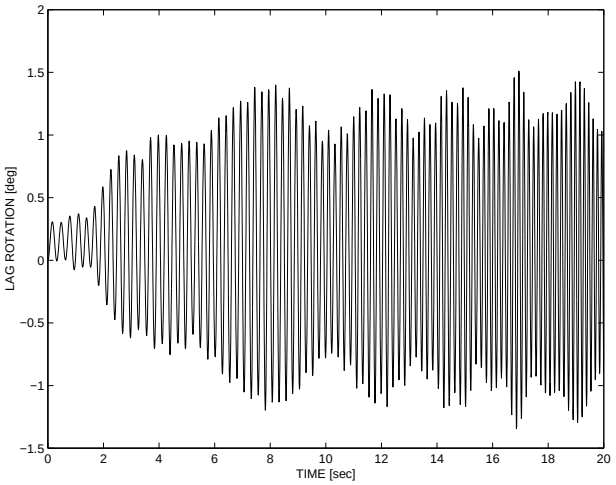

Figure 28: Time history of the relative rotations at the lag hinge.

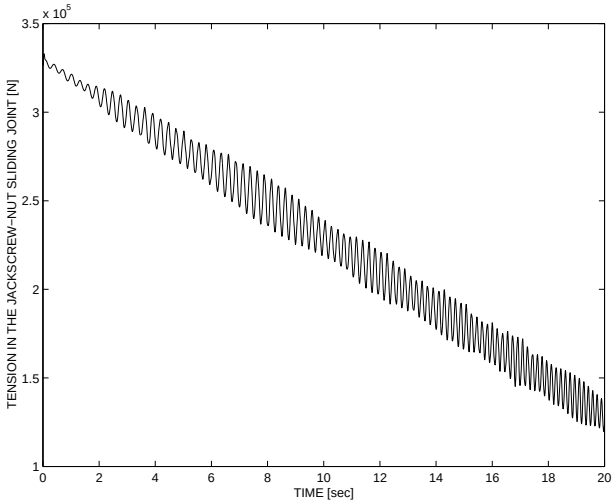

Figure 29: Time history of the force at jackscrew-nut sliding joint during blade retraction.

8 Conclusions

This paper focused on the modeling of cylindrical, prismatic, and screw joints in flexible multibody systems. In the classical formulation of these joints, kinematic constraints are enforced between the kinematic variables of the two rigid bodies. These constraints express the conditions for relative translation of the two bodies along a body-fixed axis, and imply the relative sliding of the two bodies which remain in constant contact with each other at all times. However, these kinematic constraints no longer imply relative sliding with contact when one of the bodies is flexible. In fact, when one body is elastic, the classical formulation of cylindrical, prismatic, and screw joints do no longer enforce contact between the bodies at all times.

A *sliding joint* was introduced that involves kinematic constraints at the instantaneous point of contact between the sliding bodies. In the proposed implementation, a specific node of a body is constrained to remain in contact with a beam element. This joint realistically models the piece of hardware that allows a flexible body to be in sliding contact with another. Next, a *sliding screw joint* was proposed that introduces an additional constraint on the relative rotation of the bodies. The dynamic behavior of systems with sliding mechanisms was shown to be more complex when the sliding mechanism was modeled either by a sliding or by a sliding screw joint rather than by a cylindrical, prismatic, or screw joint. This is due to the fact that for sliding joints, the sliding conditions are applied at a point that moves over the flexible member. As a result, the system configurations becomes truly variable, implying flexible members with time-varying natural frequencies.

Various numerical examples are presented that demonstrate the dramatically different behavior of the various joints in the presence of elastic bodies. In particular, the variation of the natural frequencies of the system during the simulation is captured by the sliding joint, together with the resulting changes in vibratory behavior. The proper modeling of the sliding mechanism was shown to be a prerequisite to an accurate prediction of the vibratory loads in a slider mechanism.

References

[1] J.E. Shigley and J.J. Uicker. *Theory of Machines and Mechanisms*. McGraw-Hill Book Company, New York, 1980.

[2] J.C. Simo and K. Wong. Unconditionally stable algorithms for rigid body dynamics that exactly preserve energy and momentum. *International Journal for Numerical Methods in Engineering*, 31:19–52, 1991.

[3] J.C. Simo, N. Tarnow, and M. Doblare. Non-linear dynamics of three-dimensional rods: Exact energy and momentum conserving algorithms. *International Journal for Numerical Methods in Engineering*, 38:1431–1473, 1995.

[4] J.C. Simo and N. Tarnow. A new energy and momentum conserving algorithm for the nonlinear dynamics of shells. *International Journal for Numerical Methods in Engineering*, 37:2527–2549, 1994.

[5] J.C. Simo and N. Tarnow. The discrete energy-momentum method. Conserving algorithms for nonlinear dynamics. *ZAMP*, 43:757–792, 1992.

[6] O.A. Bauchau, G. Damilano, and N.J. Theron. Numerical integration of nonlinear elastic multi-body systems. *International Journal for Numerical Methods in Engineering*, 38(16):2727–2751, 1995.

[7] O.A. Bauchau and N.J. Theron. Energy decaying scheme for non-linear beam models. *Computer Methods in Applied Mechanics and Engineering*, 134(1-2):37–56, 1996.

[8] O.A. Bauchau and N.J. Theron. Energy decaying schemes for nonlinear elastic multi-body systems. *Computers & Structures*, 59(2):317–331, 1996.

[9] C.L. Bottasso and M. Borri. Energy preserving/decaying schemes for non-linear beam dynamics using the helicoidal approximation. *Computer Methods in Applied Mechanics and Engineering*, 143:393–415, 1997.

[10] C.L. Bottasso and M. Borri. Integrating finite rotations. *Computer Methods in Applied Mechanics and Engineering*, 164:307–331, 1998.

[11] O.A. Bauchau and T. Joo. Computational schemes for nonlinear elasto-dynamics. *International Journal for Numerical Methods in Engineering*, 45(6):693–719, 1999.

[12] O.A. Bauchau. Computational schemes for flexible, nonlinear multi-body systems. *Multibody System Dynamics*, 2(2):169–225, 1998.

[13] C.L. Bottasso, M. Borri, and L. Trainelli. Integration of elastic multibody systems by invariant conserving/dissipating algorithms. Part I: formulation. *Computer Methods in Applied Mechanics and Engineering*, 190:3669–3699, 2001.

[14] C.L. Bottasso, M. Borri, and L. Trainelli. Integration of elastic multibody systems by invariant conserving/dissipating algorithms. Part II: numerical schemes and applications. *Computer Methods in Applied Mechanics and Engineering*, 190:3701–3733, 2001.

[15] O.A. Bauchau and C.L. Bottasso. On the design of energy preserving and decaying schemes for flexible, nonlinear multi-body systems. *Computer Methods in Applied Mechanics and Engineering*, 169(1-2):61–79, 1999.

[16] E.A. Fradenburgh and D.G. Matuska. Advancing tiltrotor state-of-the-art with variable diameter rotors. In *American Helicopter Society 48th Annual Forum Proceedings*, Washington, D.C., June 3-5 1992.

[17] T.R. Kane and D.A. Levinson. *Dynamics: Theory and Applications*. McGraw-Hill Book Company, New York, 1985.

Appendix A Rodrigues parameters

A common representation of finite rotations [17] is in terms of Rodrigues parameters $\underline{r} = 2\underline{u} \tan\phi/2$, where ϕ is the magnitude of the finite rotation and $\underline{u}$ the unit vector about which it takes place. The following notation is introduced

$$r_0 = \cos^2 \frac{\phi}{2} = 1 \ / \ (1 + \frac{\underline{r}^T \ \underline{r}}{4}). \tag{A1}$$

The finite rotation tensor R is

$$R(\underline{r}) = I + r_0 \ \widetilde{r} + \frac{r_0}{2} \ \widetilde{r} \ \widetilde{r}; \tag{A2}$$

The relationship between the angular velocity vector $\underline{\omega}$ and the time derivative of Rodrigues parameters is $\underline{\omega} = H \ \dot{\underline{r}}$, where

$$H(\underline{r}) = r_0(1 + \frac{1}{2} \ \widetilde{r}). \tag{A3}$$

Matrices R and H are endowed with the following properties

$$RR^T = I; \quad R \ \underline{r} = \underline{r}; \quad R = HH^{-T} = H^{-T}H; \tag{A4}$$

$$R = (I + \frac{\widetilde{r}}{2}) \ \frac{R+I}{2} = \frac{R+I}{2} \ (I + \frac{\widetilde{r}}{2}) \tag{A5}$$

$$I = (I - \frac{\widetilde{r}}{2}) \ \frac{R+I}{2} = \frac{R+I}{2} \ (I - \frac{\widetilde{r}}{2}) \tag{A6}$$